Integrated plasma equipment model for polysilicon etch profiles in an inductively coupled plasma reactor with subwafer and superwafer topography

Robert J. Hoekstra,[a] Michael J. Grapperhaus,[b] and Mark J. Kushner[c]
Department of Electrical and Computer Engineering, University of Illinois, Urbana, Illinois 61801

(Received 11 October 1996; accepted 14 March 1997)

Above wafer topography of the substrate, such as wafer clamps, is known to impact adjacent feature profiles during plasma etching of microelectronic devices. The consequences of subwafer topography, such as electrostatic chucks and cooling channels, on feature profiles is less well characterized. To investigate these issues we have developed and integrated a plasma equipment model and a Monte Carlo feature profile model, and applied the integrated model to investigate polysilicon etching in an inductively coupled plasma reactor. We find that, when using low conductivity wafers, subwafer topography reduces the sheath potentials above the wafer which results in lower ion energies incident on the wafer. Etch rates sensitive to ion power are therefore also reduced. Due to the perturbation of the presheath and sheath, subwafer topography can also affect the angular distribution of the ion flux incident on the wafer which then results in asymmetric etch profiles. Superwafer structures perturb both the magnitude and angular distribution of the ion flux due to shadowing at the edge of the wafer. This leads to lower etch rates and asymmetric etch profiles. Inhibitor fluxes can be used to control the etch profile shape but only at relatively low magnitudes of those fluxes. © *1997 American Vacuum Society.* [S0734-2101(97)06204-0]

I. INTRODUCTION

Plasma etching is standard practice in the semiconductor industry for microelectronics manufacturing to fabricate narrow ($<0.5\ \mu$m) features and to meet the demand for greater anisotropy of etch profiles.[1] Development of etch processes that uniformly yield highly anisotropic profiles across the full diameter of the wafer has been complicated by their sensitivity to local reactor operating conditions and to the topography of the substrate. For example, it is common to find that the substrate beneath the wafer has nonplanar topography such as gas cooling channels or components of electrostatic chucks. It has been observed that etch rates of SiO_2 are lower at locations that mirror the gas cooling channels under the wafer.[2] A similar effect has been observed in the etching of flat panel display substrates.[3] In both cases, the observations cannot be attributed to wafer temperature variations above these structures. These observations place added importance on simulating etch processes using an integrated modeling approach that accounts for the plasma properties, as well as details of the substrate topography. In this manner one can evaluate the consequences of reactor topography and the material properties of structural components on etch profiles in a self-consistent manner.

To address these issues, an integrated plasma equipment-etch profile model was developed to enable one to assess the impact of structural components of the reactor on etch profiles. The integrated model links a comprehensive plasma equipment model with an etch profile simulator. The Monte Carlo feature profile model (MC-FPM), which was developed for this study, predicts etch profiles as a function of position on the wafer using the ion and neutral flux distributions (angle and energy) which are produced by the plasma equipment model. As a demonstration of the linkages of subwafer and superwafer topography with etch profiles, we used the integrated model to simulate the etching of polycrystaline silicon (poly-Si) in an inductively coupled plasma (ICP) reactor using an Ar/Cl_2 gas mixture. The test reactor has subwafer structures, in the form of dielectric channels, and superwafer structures, in the form of wafer clamps. The subwafer structures are intended to simulate the effects of cooling channels or components of an electrostatic chuck. It was found that the superwafer structures perturb the angular distribution of the incident ions, thereby modifying the etch profile, and they reduce the magnitude of the ion flux, thereby reducing the etch rate. The major effect of subwafer structures is to decrease ion energies thereby decreasing etch rates for ion driven processes.[4] There is also a broadening of the ion angular distribution due to the lowered ion energies and an asymmetry in the ion angular distribution due to perturbation of the presheath and sheath electric fields. Including inhibitor or passivation fluxes was found to remediate sidewall etching due to these broadened ion angular distributions, thereby reducing asymmetries in the feature. The passivation also slows lateral thermal etch rates in poly-Si due to high doping. The isotropy and symmetry of etch profiles are more sensitive to superwafer topography since these structures more significantly perturb the presheath and there-

[a]Electronic mail: stretch@uigela.ece.uiuc.edu
[b]Electronic mail: grapper@uiuc.edu
[c]Electronic mail: mjk@uiuc.edu

fore affect the directionality of ions entering the sheath to a greater extent.

The integrated plasma equipment-profile model will be described in Section II, followed by a discussion in Section III of results from the model for etching of poly-Si in Ar/Cl_2 plasmas. Our concluding remarks are in Section IV.

II. DESCRIPTION OF THE INTEGRATED PLASMA EQUIPMENT-FEATURE PROFILE MODEL

The integrated plasma equipment-feature profile model consists of three major components: the hybrid plasma equipment model (HPEM), the plasma chemistry Monte Carlo simulation (PCMCS) and the MC-FPM. The HPEM is a two-dimensional, modular simulation, that combines an electromagnetic module, an electron kinetics module, and a fluid model in an iterative fashion. The HPEM produces electric fields, ion and neutral densities as a function of position, and ion and neutral fluxes incident on to the wafer. The electric potential throughout the reactor (both in the plasma and through material structures) is solved, thereby enabling one to assess the effects of reactor topography and construction materials on plasma properties. The HPEM, as used in this study, is described in detail in Refs. 5 and 6. Ion and neutral momentum equations are included for all heavy particle species.

A semi-analytic sheath model was also integrated into the HPEM to more realistically represent the fields and fluxes at gas-solid boundaries under conditions where the actual sheath thickness is less than the mesh spacing. The sheath model tracks the charging and discharging of the sheath during the radio frequency (rf) cycle assuming collisionless transversal by the ions through the sheath and a Boltzmann distribution for the electrons. The voltage drop across the sheath is produced by the semi-analytic sheath model, which is then applied as a jump condition in solving Poisson's equation for the entire reactor. The sheath model is described in Ref. 7.

The HPEM uses a fluid model for heavy particle transport, and so particle energy distributions (PEDs) and particle angular distributions (PADs) for neutrals and ions striking the wafer are not directly available. These distributions are produced by the PCMCS. The PCMCS, described in Ref. 8, calculates the trajectories of neutral and ion plasma species in the gas phase and their collisions with surfaces. It uses the sources of plasma species, time dependent electric fields, and time dependent sheath properties generated by the HPEM. The PCMCS produces PEDs and PADs of all plasma species intersecting with all surfaces, including the wafer. The MC-FPM then uses these PADs and PEDs as a function of position on the wafer to generate etch profiles.

The two-dimensional MC-FPM uses Monte Carlo methods to evolve an etch profile based on the fluxes, PADs, and PEDs generated by the PCMCS. There are a number of published profile models that use analytic methods to resolve the features of the profile with arbitrarily fine spatial resolution,[9–11] and in that sense are more versatile than Monte Carlo based models. We chose to use a Monte Carlo method due to the ease of implementing surface reaction mechanisms of user defined complexity and which are energy dependent.

The MC-FPM resolves the trench region on the wafer (mask and semiconductor) in two dimensions using a rectilinear mesh. The mesh spacing is typically 200 cells for 1 μm length. Each computational cell is therefore about 15 $\times$15 atoms. Each cell is assigned a material identity (e.g., poly-Si, photoresist, SiO_2, plasma) which may change during the simulation. Gas phase species (i.e., radicals and ions) are represented by computational pseudoparticles. Solid species, including adsorbates or passivation, are represented by the identity of the computational cell. The MC-FPM begins by launching pseudoparticles representing radicals and ions towards the surface with initial trajectories (energy and angle) randomly chosen from the PEDs and PADs provided by the PCMCS. The pseudoparticles are launched with a frequency computed from the total flux of radicals or ions incident on the substrate so that each pseudoparticle represents the approximate number of solid atoms in a single computational cell. The pseudoparticle trajectories are advanced in time using a second order Runge-Kutta technique. The effects of surface charging on the profile evolution are not addressed here. In cases of surface charging and ion acceleration due to the electric field in the trench there is a slight narrowing of the trench due to ''focusing'' of the ions by the positively charged sidewalls. This effect lessens as the conductivity of the poly-Si increases. The details of surface charging do not impact the thrust and conclusions of this article.

A generalized reaction scheme for interaction of the ions and neutrals with the surface is used in the MC-FPM which allows for any reactant-product combination, and allows for an energy dependence of the interaction. These processes are input to the MC-FPM through a file which lists the reactions in conventional chemical notation [e.g., Cl(g) + Si(s) $\rightarrow$ SiCl(s)]. This file is preprocessed to construct probability arrays for the reaction of pseudoparticle plasma species with surface species. The classes of reactions in the model include adsorption, passivation, ion activated etching, thermal etching, sputtering, ion or neutral reflection, and re-emission. When a pseudoparticle impacts on a surface, the reaction that occurs is chosen from the probability arrays using Monte Carlo techniques. Based on this reaction, the material identity of the computational cell at the site of impact is appropriately changed. Particles which are desorbed or re-emitted from the surface are given thermal speeds and launched with a Lambertian angular distribution, or reflected as a neutral in the case of an ion. The trajectory of etch or re-emission products are then tracked as pseudoparticles in the manner described by the reaction mechanism. Unless otherwise noted, the photoresist is considered a hard mask having a low etch rate.

The polysilicon etch mechanism we have adopted is based on the works of Cheng *et al.*[12] and Meeks.[13] Etching takes place by first successively chlorinating the polysilicon surface, forming $SiCl_n$ (i.e., SiCl followed by $SiCl_2$, and so on).

TABLE I. Surface reactions for the poly-Si etch mechanism.

Reaction[a]	Probability for reaction[b]	Reference
$Si_{(s)}+Cl_{(g)}\rightarrow SiCl_{(s)}$	0.99	13
$SiCl_{(s)}+Cl_{(g)}\rightarrow SiCl_{2(s)}$	0.20	13
$SiCl_{2(s)} + Cl_{(g)} \rightarrow SiCl_{3(s)}$	0.15	13
$SiCl_{3(s)} + Cl_{(g)} \rightarrow SiCl_{4(g)}$	0.0001	13[c]
$Si_{(s)} + SiCl_{2(g)} \rightarrow Si_{(s)} + SiCl_{2(s)}$	0.8	13
$SiCl_{(s)} + SiCl_{2(g)} \rightarrow SiCl_{(s)} + SiCl_{2(s)}$	0.5	13
$SiCl_{2(s)} + SiCl_{2(g)} \rightarrow SiCl_{2(s)} + SiCl_{2(s)}$	0.3	13
$SiCl_{3(s)} + SiCl_{2(g)} \rightarrow SiCl_{3(s)} + SiCl_{2(s)}$	0.1	13
$SiCl_{2(s)} + Ar^{+} \rightarrow SiCl_{2(g)} + Ar_{(g)}$	$0.16\,\frac{(\epsilon-\epsilon_o)^{1/2}}{\epsilon_o^{1/2}}$	12[d]
$SiCl_{3(s)} + Ar^{+} \rightarrow SiCl_{3(g)} + Ar_{(g)}$	$0.16\,\frac{(\epsilon-\epsilon_o)^{1/2}}{\epsilon_o^{1/2}}$	12[d]
$SiCl_{(s)} + Cl^{+} \rightarrow SiCl_{2(g)}$	$0.13\,\frac{(\epsilon-\epsilon_o)^{1/2}}{\epsilon_o^{1/2}}$	12[d]
$SiCl_{2(s)} + Si_{(s)} + Cl^{+} \rightarrow SiCl_{2(g)} + SiCl_{(s)}$	$0.16\,\frac{(\epsilon-\epsilon_o)^{1/2}}{\epsilon_o^{1/2}}$	12[d]
$SiCl_{3(s)} + Cl^{+} \rightarrow SiCl_{4(g)}$	$0.19\,\frac{(\epsilon-\epsilon_o)^{1/2}}{\epsilon_o^{1/2}}$	12[d]
$Si_{(s)} + Cl_2^{+} \rightarrow SiCl_{2(g)}$	$0.13\,\frac{(\epsilon-\epsilon_o)^{1/2}}{\epsilon_o^{1/2}}$	12[d]
$SiCl_{(s)} + Si_{(s)} + Cl_2^{+} \rightarrow SiCl_{2(g)} + SiCl_{(s)}$	$0.16\,\frac{(\epsilon-\epsilon_o)^{1/2}}{\epsilon_o^{1/2}}$	12[d]
$SiCl_{2(s)} + Si_{(s)} + Cl_2^{+} \rightarrow SiCl_{2(g)} + SiCl_{2(s)}$	$0.16\,\frac{(\epsilon-\epsilon_o)^{1/2}}{\epsilon_o^{1/2}}$	12[d]
$SiCl_{3(s)} + Si_{(s)} + Cl_2^{+} \rightarrow SiCl_{4(g)} + SiCl_{(s)}$	$0.19\,\frac{(\epsilon-\epsilon_o)^{1/2}}{\epsilon_o^{1/2}}$	12[d]

[a]Subscript (s) denotes a surface species. Subscript (g) denotes a gas or plasma species.
[b]ϵ is the ion energy. $\epsilon_o=10$ eV unless noted otherwise.
[c]Thermal etch probability was varied for some cases as noted.
[d]Reaction mechanism was derived from the cited reference. The precise values for probabilities were modified.

This chlorination is predominantly accomplished by neutral Cl atoms. Etching of the poly-Si and evolution of the $SiCl_n$ etch product then occurs through subsequent ion bombardment. A summary of the reaction scheme and reaction probabilities used in the model appears in Table I. The probability for an ion of energy ϵ activating an etch scales as $(\epsilon-\epsilon_0)^{1/2}$, where ϵ_0 is a threshold energy.[12] In addition to the reactions appearing in Table I, we also allowed there to be an inhibitor flux which deposits on surfaces thereby blocking the etch. The inhibitor is removed by ion bombardment. The inhibitor flux is intended to represent polymerization which may be produced from sputtered mask material or other gas phase species. We also allow the polysilicon to be thermally etched by Cl atoms in the absence of ion bombardment, as may occur at high doping levels. The silicon dioxide underlayer to the poly-Si is etched with an arbitrarily chosen selectivity of 1:50 relative to poly-Si. This is achieved by using a reaction mechanism analogous to that for poly-Si with reduced etch probabilities. Cl can also reassociate on chlorinated surfaces in the trench to produce Cl_2, however for the cases presented here Cl reassociation was not included. We did run test cases with this process using reaction probabilities of 0.02 for $SiCl_2$ and 0.08 for $SiCl_3$ based on the work of Meeks.[13] Including Cl reassociation *in the trench* has a negligible effect on the etching characteristics due to its low rate compared to Si chlorination and etching.

III. PREDICTED ETCH PROFILES AND RATES WITH SUBSTRATE AND SUPERWAFER TOPOGRAPHY

The geometry we used in this study is an ICP reactor using a flat spiral four turn coil set on a quartz window [see Fig. 1(a)]. This reactor is described in detail in Ref. 5. The process parameters we used are an $Ar/Cl_2=70/30$ gas mixture flowing at 150 sccm with 1 kW of ICP power at 13.56 MHz and a 150 V bias also at 13.56 MHz applied to the substrate. The gas-phase plasma chemistry reaction mechanism we used is described in Ref. 5 as are typical plasma conditions. Computed peak ion and Cl radical densities for our test parameters are 6.36×10^{11} cm^{-3} and 8.12×10^{13} cm^{-3}, respectively. The 20 cm diameter wafer is modeled as silicon with a specified conductivity, a thin over coating of SiO_2, poly-Si and photoresist. The subwafer structure is a dielectric ring with permittivity of $\epsilon/\epsilon_0=1.0$ located beneath and in contact with the wafer between radii of 4.5 and 6.25 cm. The superwafer topography is a clamp covering the outer 0.25 cm of the wafer. The dielectric ring approximates the effect of subwafer structures such as cooling channels or as might be used in the construction of an electrostatic chuck. Etch properties will be discussed at the three radial locations noted in Fig. 1(a). These locations are (1) an open field site at a radius of $r=3$ cm which is not affected by topography, (2) near the outer radius of the subwafer dielectric at $r=6.0$ cm, and (3) near the clamp at $r=9.625$ cm. Etch profiles were simulated for a resist opening of 0.6 μm, a hard mask thickness of 0.2 μm, a 0.7 μm poly-Si layer, and an oxide etch stop layer of 0.1 μm, as schematically shown in Fig. 1(b).

The total ion and chlorine radical fluxes incident onto the wafer are shown in Fig. 2 as a function of radius. Their values at the inspection points and the corresponding etch rates are shown in Table II. The etch rate is an average value given by the vertical distance etched divided by the etch time. Due to significant dissociation of the Cl_2 feedstock, the major ion incident on the wafer is Cl^+. As a result of its higher ionization potential and rapid charge exchange to Cl_2^+ and Cl^+, the flux of Ar^+ is only 10% of the total. The magnitudes of the ion and radical fluxes are uniform to within about 10% to a radius beyond the dielectric ring. Adjacent to the clamp, the ion flux falls to approximately half its peak value, while the Cl atom flux decreases by 20%. There is a small peak in the ion flux at a radius of 5–6 cm due to the maximum in power deposition by the torroidal electric field. The PAD and PED for Cl atoms are essentially uniform across the radius with a small decrease in magnitude near the clamp due to shadowing. This results from the low reactive sticking coefficient (<0.01) for Cl on nonsilicon surfaces. The PED is essentially thermal with a small high

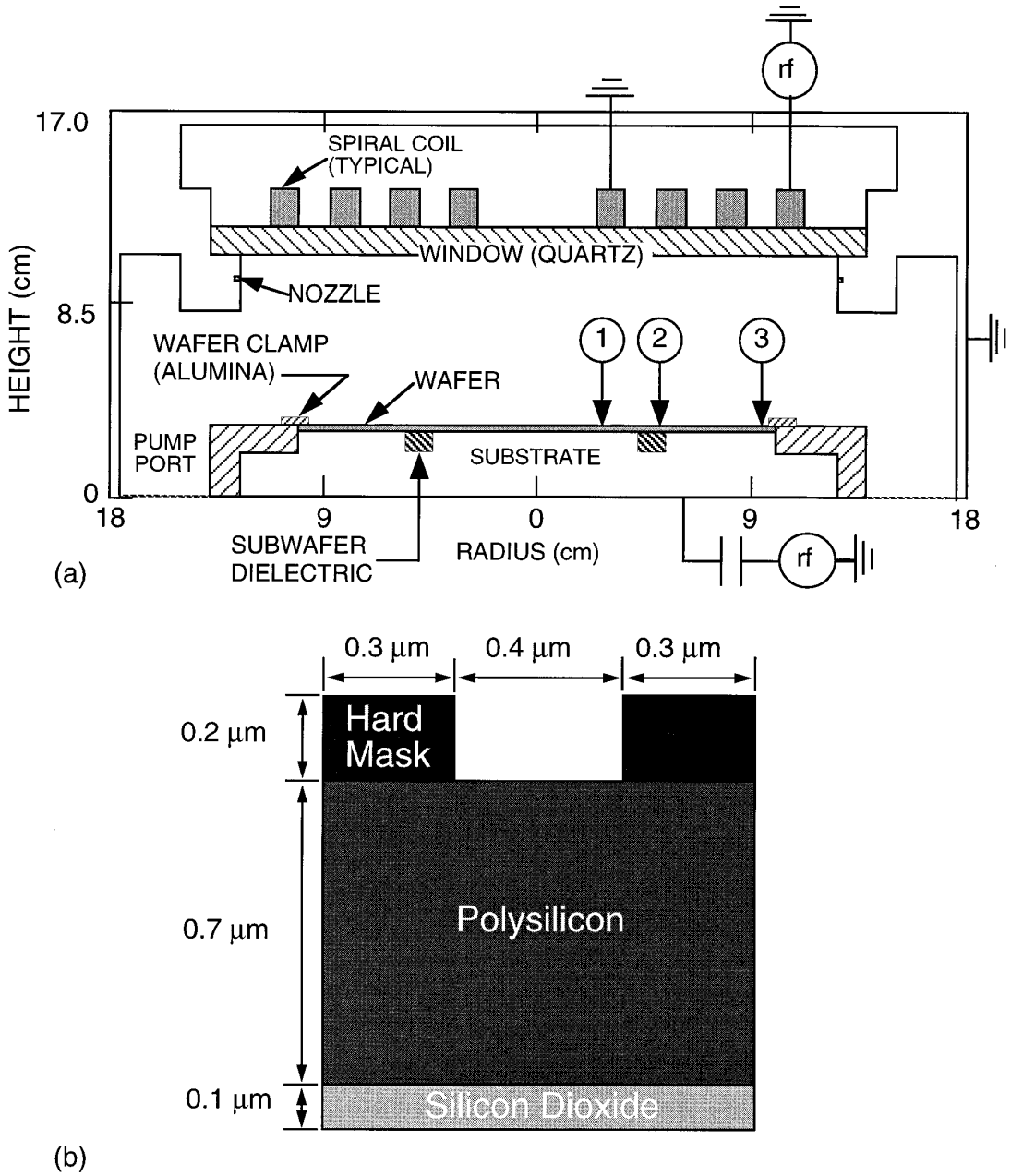

FIG. 1. (a) Schematic of the ICP reactor used in this study. (b) Initial feature profile.

energy tail extending to a few eV resulting from charge exchange with energetic ions. The PAD is essentially isotropic. The Cl radical flux is composed of 10% excited states although our etch mechanism is not sensitive to the excitation state of the radical.

The PED and PAD for the total ion flux striking the wafer at the three inspection points are shown in Fig. 3. For these cases, the wafer is treated as a perfect dielectric. The PED in the open field has the characteristic double-peaked shape associated with the thin sheaths encountered in high plasma density reactors.[8] The ions acquire 0.5–1 eV of transverse energy crossing the presheath,[14] which then requires ion acceleration across the sheath of >10s V depth to straighten into anisotropic trajectories. The PAD is therefore generally broader at the lower energies of the PED where insufficient ion acceleration has occurred to counter the transverse component of ion energy entering the sheath. The major consequence of the subwafer dielectric is to reduce the sheath potential in the plasma at the surface of the wafer above the dielectric, thereby reducing the average ion energy to the substrate (see Table II). As discussed in Ref. 4, the subwafer dielectric acts as a capacitor which charges and discharges during the rf cycle, thereby garnering voltage that would have otherwise been dropped across the wafer or across the sheath. The sheath potential is therefore smaller above the dielectric, which then shifts the PED to lower energies. For

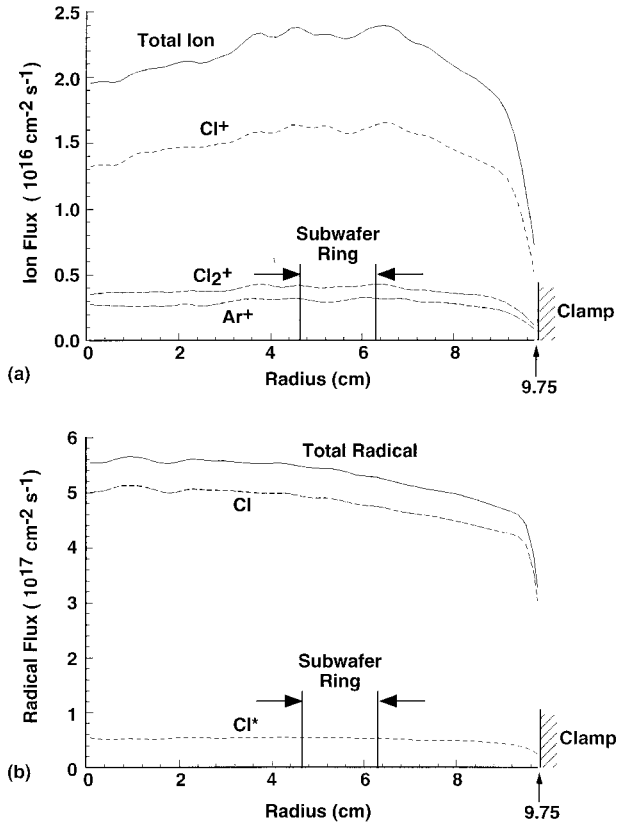

FIG. 2. Fluxes of plasma species striking the wafer as a function of radius for the ICP reactor using an $Ar/Cl_2 = 70/30$ gas mixture, 10 mTorr, 1 kW of ICP power and 150 V bias on the substrate. (a) Ion fluxes and (b) Cl radical fluxes.

these conditions, the drop in average ion energy is from 68 eV (at locations far from the dielectric) to 49 eV (above the dielectric). In principle, the subwafer dielectric should not have a major effect on the PAD, since the remaining sheath potential is generally sufficient to redirect ions vertically into the substrate. The two-dimensional nature of the presheath, though, cause significant perturbations to the PED and PAD.

The ion PAD/PED for the location above the subwafer dielectric shown in Fig. 2(b) is asymmetric, having an offset to negative angles. It is also somewhat broader than that at the open field location. The broadening of the PAD results from the lower ion energy caused by the reduced sheath potential as described above. The asymmetry results from radial gradients in the presheath. The location at which this PAD is recorded is towards the outer edge of the subwafer

TABLE II. Reactant and etch characteristics at the inspection points.

	Radius (cm)		
	3.0	6.0	9.625
Total ion flux ($cm^{-2}\ s^{-1}$)	2.2×10^{16}	2.3×10^{16}	1.2×10^{16}
Average ion energy (eV)	68	49	69
Cl atom flux ($cm^{-2}\ s^{-1}$)	5.6×10^{17}	5.4×10^{17}	3.9×10^{17}
Poly-Si etch rate (Å/min)	1800	1350	760

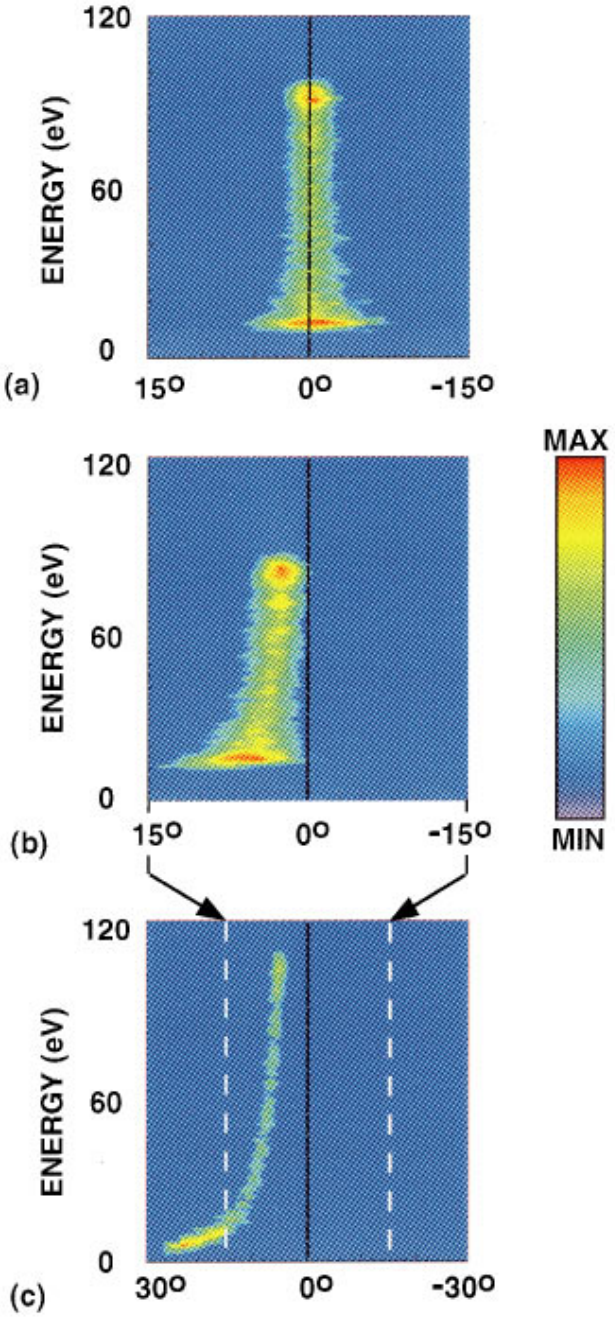

FIG. 3. Total ion energy and angular distribution striking the wafer for (a) the open field ($r = 3$ cm) which is representative of locations further than 1 cm from the subwafer dielectric or clamp, (b) above the subwafer dielectric ($r = 6$ cm), and (c) adjacent to the wafer clamp ($r = 9.625$ cm). Due to voltage division between the sheath and subwafer dielectric, the ion energy distribution is cut off. The angular distributions above the dielectric and near the clamp are asymmetric due to perturbation of the presheath.

dielectric. The sheath potential is lowest at the midpoint of the dielectric, and increases to its open field value towards the edges of the dielectric. As a result, the sheath potential has a radial gradient, which in turn produces a transverse electric field in the presheath. The ions therefore enter the sheath with a net positive radial velocity. (On the inner side of the subwafer dielectric, the presheath produces a net negative radial ion velocity.) The asymmetry we observe in the

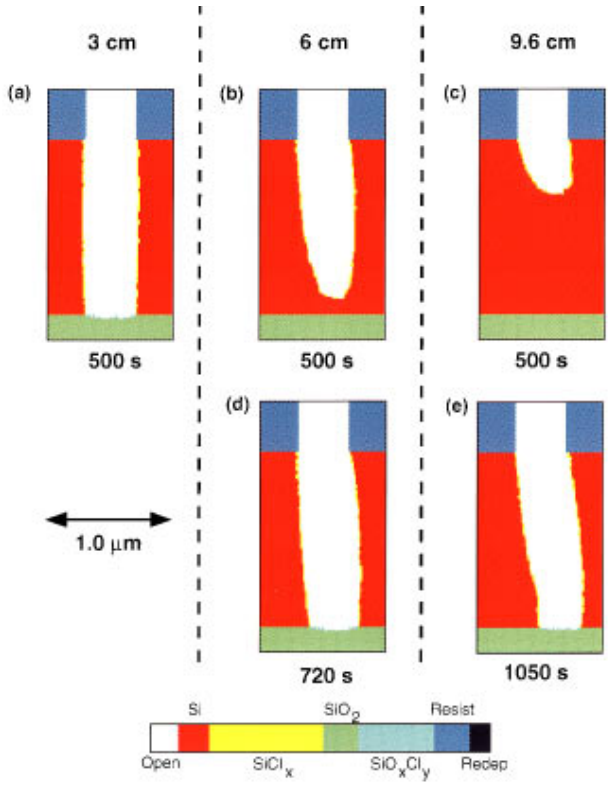

FIG. 4. Feature profiles after a 500 s etch for (a) open field ($r=3$ cm), (b) above the subwafer dielectric ($r=6$ cm), and (c) adjacent to the clamp ($r=9.625$ cm). Fully developed etch profiles for (d) $r=6$ cm (after a 720 s etch) and (e) $r=9.625$ cm (after a 1050 s etch). The asymmetric ion angle distributions produce a slanted etch profile.

PAD results from there being insufficient sheath voltage to straighten the ion trajectories to the vertical. For this reason the angular offset is most prominent at low ion energies, and less severe at higher energies where additional sheath voltage is available to straighten the trajectories. The PAD/PED near the clamp has an even more severe asymmetry for essentially the same reason. The vertical clamp face produces a net radial electric field in the presheath which results in a net positive radial velocity for ions entering the sheath.

Predicted poly-Si etch profiles obtained with the MC-FPM after 500 s of etching are shown in Figs. 4(a), 4(b), and 4(c) for the open field, over the subwafer dielectric and near the clamp, respectively. For these cases, there is no inhibitor flux. The etch profile in the open field is anisotropic with straight walls and clean corners. The etch rate at this location is 1800 Å/min. Our etch mechanism proceeds through an intermediate step where Cl atoms chlorinate the surface, forming $SiCl_x$ species shown in yellow. $SiCl_x$ is removed from the surface by ion bombardment, and is therefore less prevalent near the bottom of the trench. This profile is representative of all wafer locations more than 1 cm distant from either the subwafer dielectric or the wafer clamp.

Product fluxes returning to the plasma from the trench were examined at the 3.0 cm radical location. In all cases, the fluxes returning to the plasma are dominated by Cl atoms resulting from either Cl that did not react on the surface or from the neutralized products of ion recombination. Early during the etch, the reactivity of Cl is high due to chlorination of the surface and the ratio of the Cl flux to the $SiCl_x$ flux leaving the trench is 40:1. After the surface is chlorinated, the ratio increases to as large as 600:1. When the oxide layer is reached, there is a decrease in $SiCl_x$ flux (some etching of the side wall continues to produce $SiCl_x$) and a small SiO_xCl_y flux appears as the oxide layer begins to etch at a lower rate. At this point the product flux ratios for $Cl:SiCl_x:SiO_xCl_y$ are 2000:2:1.

The reduced ion energy at locations above the dielectric lowers the etch rate compared to the open field position, in this case to 1350 Å/min. The etch has had insufficient time to reach the SiO_2. If the polysilicon is doped *n* type the thermal etch rate by Cl atoms will be large. Since the Cl radical flux above the dielectric is essentially the same as that for the open field, the lower ion energy above the dielectric results in a lower vertical to horizontal etch rate, dropping to as low as 5:1 in the absence of side wall passivation. This produces rounded side walls, as shown in Fig. 4(b). An analogous situation occurs near the wafer clamp where the etch rate is still lower, 760 Å/min. Here the reduced etch rate results primarily from a lower ion flux (as opposed to lower ion energy), approximately half that near the center of the wafer. The etch profiles for the above dielectric and near clamp locations after 500 s show indications of some increased undercutting due to the broadening of the PAD and an asymmetry due to the angular offset in the PAD.

The lower etch rates over the dielectric and near the wafer clamp require longer times to clear the bottom of the trench. The etch profiles obtained at these sites when the width of the trench at its base is approximately equal to the resist opening are shown in Figs. 4(d) and 4(e). The etch times are 720 and 1050 s, respectively. Since the width of the PAD is not overtly perturbed by the subwafer dielectric, the width of the etch profile over the dielectric is similar to that of the open field with some small amount of additional undercutting due to the reduction in the vertical-to-horizontal etch rate. However, the angular offset of the PAD produces an asymmetric etch profile with more undercutting on the wall at the outer radius. The effect is more severe near the wafer clamp where the angular offset in the ion flux is more pronounced. The addition of an inhibitor flux can help lower the horizontal etch rate and narrow the profile. However the improvement is not as dramatic as at open field locations since there is now an increased ion flux to the side walls which removes the inhibitor. Deposition of an inhibitor on the base of the trench does also occur, which decreases the vertical etch rates leading to longer etch times, but the effect is not large due to the more rapid rate of removal by ion bombardment.

The degree of asymmetry of the etch profile above the subwafer dielectric increases with increasing etch depth. For example, etch profiles are shown in Fig. 5 in the open field ($r=3$ cm) and above the subwafer dielectric ($r=6$ cm) for trench depths of 0.7, 1.4, and 2.1 μm. In all cases, the etch profile in the open field remains anisotropic, with some small

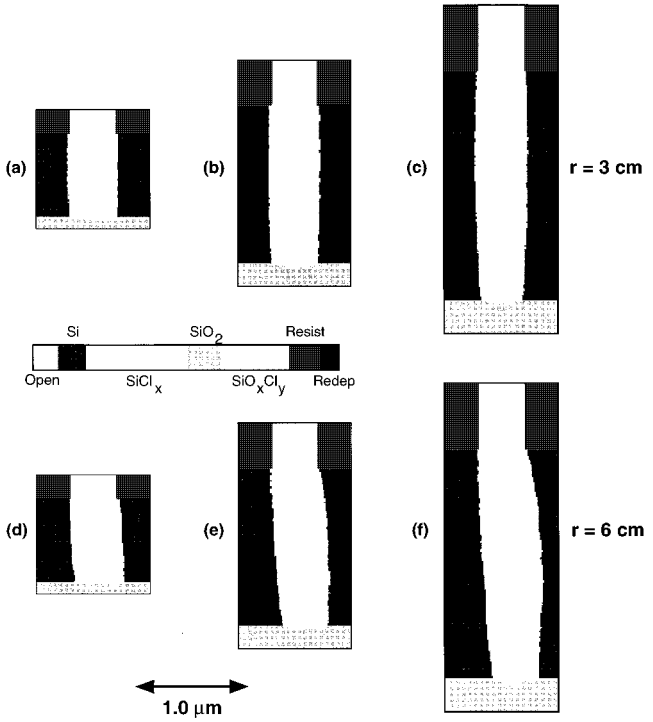

FIG. 5. Etch profiles at $r=3$ cm (open field) for aspect ratios of (a) 1:1, (b) 1:2, and (c) 1:3. Profiles at $r=6$ cm (above the dielectric) for aspect ratios of (d) 1:1, (e) 1:2, and (f) 1:3.

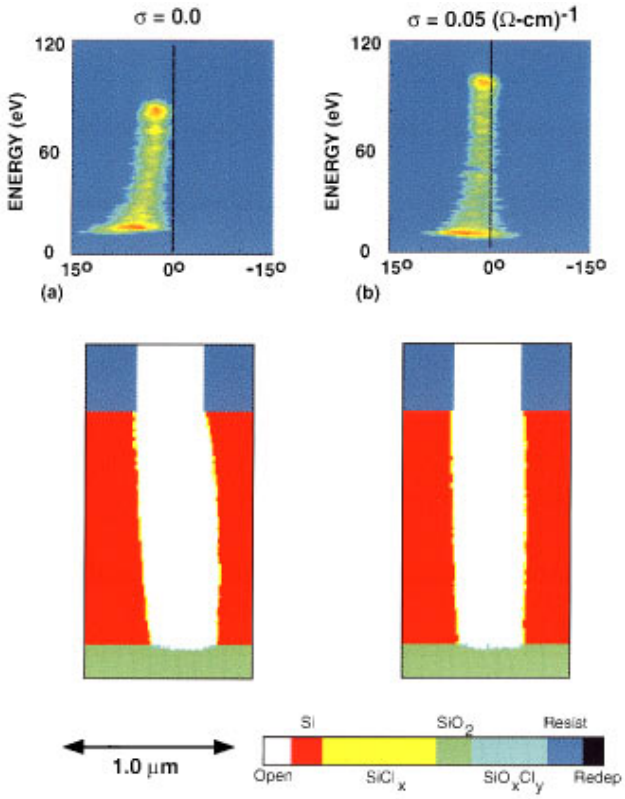

FIG. 6. Comparison of etch profiles and total ion PAD/PED above the subwafer dielectric ($r=6$ cm) with (a) a perfect dielectric wafer and (b) a wafer with conductivity $=0.05\ \Omega^{-1}\ \mathrm{cm}^{-1}$. The higher conductivity wafer shields the plasma from electrical nonuniformities below the wafer.

amount of bowing for the deepest trench due to an uninhibited lateral thermal etch. Above the subwafer dielectric where the PAD/PED is perturbed and asymmetric, the etch profile is increasingly offset as the depth increases, although the slope of the inner wall is essentially the same. With increasing depth and etch time, the outer wall becomes increasingly more bowed.

The perturbation of the ion flux by subwafer dielectrics is a function, in part, of the electrical properties of a wafer. For example, a highly conductive wafer would appear to be an equipotential plane that electrically shields the plasma from structures below the wafer. The consequences of subwafer dielectrics are, then, most severe for lightly doped wafers having largely dielectric properties. As a demonstration of this effect, the total ion PAD/PED and etch profiles above the dielectric ring are shown in Fig. 6 for a perfect dielectric wafer and for a wafer conductivity of $0.05\ \Omega^{-1}\ \mathrm{cm}^{-1}$ without the use of an inhibitor flux. With the higher conductivity wafer, the plasma is largely electrically shielded from the subwafer topography. As a result there is less perturbation of the sheath and presheath. The PAD and PED more closely resemble the open field distributions although there is still an angular offset. Although there is some amount of undercutting, the larger ion energy obtained with the more conductive wafers increases the vertical etch rate to the open field value and recoups the anisotropic nature of the etch in spite of the uninhibited lateral thermal etch rate. However, there does remain a small asymmetry due to capacitive perturbation of the sheath and presheath.

The spontaneous thermal etching of n-type poly-Si can produce a significant undercutting of the mask and broadening of the etch profile. For example, the etch profile at $r=6.0$ cm (above the dielectric) is shown in Fig. 7(a) for a dielectric wafer, without an inhibitor flux and without thermal etching. In Fig. 7(b), the spontaneous thermal etch probability by Cl atoms is 0.5%, which causes an increase in

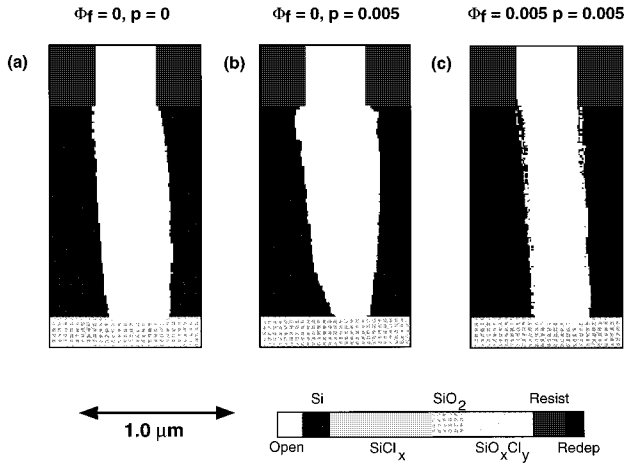

FIG. 7. Etch profiles above the subwafer dielectric ($r=6$ cm) for different combinations of the inhibitor flux, ϕ_f, and thermal Cl etch probability p. ϕ_f is expressed as a fraction of the Cl atom flux. (a) $\phi_f=0.0$, $p=0.0$, (b) $\phi_f=0.0$, $p=0.005$, (c) $\phi_f=0.001$, $p=0.005$.

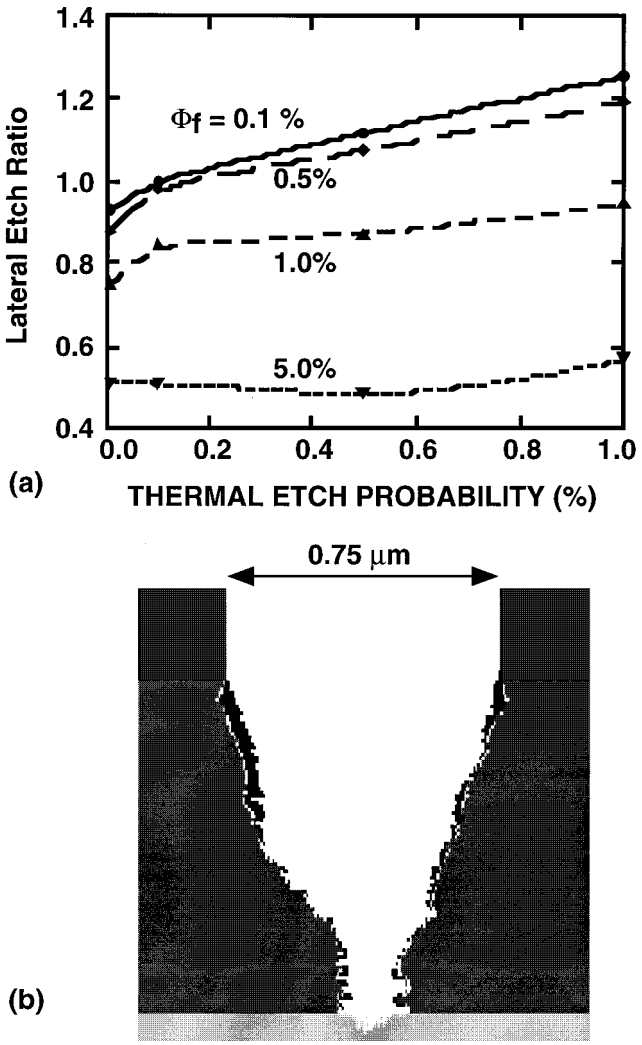

FIG. 8. (a) Etch profile shape factor [(average feature width)/(mask width)] as a function of the Cl atom thermal etch probability. Shape factors are shown for different values of the inhibitor flux, f, expressed as a fraction of the Cl atom flux. (b) With large fluxes of the inhibitor flux, the feature profile takes on a wedge shape.

undercutting due to the broad PAD of the Cl atom flux. The anisotropic etch profile is recouped with an inhibitor flux that is 0.1% that of the Cl atom flux, as shown in Fig. 7(c).

The requirement for an inhibitor flux to produce anisotropic profiles is ultimately a function of the lateral-to-vertical etch rate which in turn is a function of the PED/PAD and thermal etch rate. For a given thermal etch rate, however, there is an inhibitor flux producing side wall passivation which yields straight wall features. To illustrate this relationship we defined a lateral etch ratio R as (average trench width)/(mask opening width). R as a function of thermal etch probability and inhibitor flux is shown in Fig. 8(a). When the lateral etch is large due to high thermal etch rates, R is large due to undercutting. Increasing inhibitor fluxes recoups the straight wall feature ($R=1$). However large inhibitor fluxes eventually cause loss of critical dimension, leading to narrowed features as seen in Fig. 8(b). We found that, for a small thermal etch probability, an inhibitor flux 0.1% of the Cl atom flux gives the most satisfactory trench profiles.

IV. CONCLUDING REMARKS

We have investigated the etching of polysilicon in argon/chlorine gas mixtures in a high plasma density inductively coupled reactor. Subwafer topography, such as electrostatic chucks, can have significant effects on the etch rate due to a reduction of the ion energy incident on the wafer. The etch profile can be perturbed due to an asymmetry in the ion angular distributions caused by perturbations to the sheath and presheath. This effect is most severe when using wafers having low conductivity. In cases where the polysilicon is heavily n type, the thermal etch rate is large, thereby lowering the vertical-to-horizontal etch selectivity. This effect is most severe above subwafer structures where the vertical etch rate is already low due to the smaller ion energies. Inhibitor fluxes are therefore required to recoup vertical-to-horizontal selectivity. When wafer clamps are used, the adjacent ion flux is low and the ion angular distribution is broadened with an imposed asymmetry due to shadowing and perturbation of the presheath. Analogous to the location above the dielectric, the etch rate is lower and the etch profile may be asymmetric. The lowering of the ion energy distribution or ion flux and perturbation of the PAD by substrate topography both contribute towards decreasing the vertical-to-lateral etch rate, particularly when there is a significant neutral driven etch rate that is otherwise unaffected. The reduction in the vertical-to-lateral etch rate requires both longer etch times (pushing other wafer locations into an overetch situation) and increased inhibitor fluxes to recoup the desired anisotropy. The deleterious effects of subwafer topography are less severe with high conductivity wafers which electrically shield the plasma from nonuniformities in the substrate.

Note added in proof: Ion energy and angle distributions have recently been reported by J. R. Woodworth, B. P. Aragon, and T. W. Hamilton [Appl. Phys. Lett. **70**, 1947 (1997)] for cases where superwafer topography was added to the substrate. The superwafer topography consisted of a ceramic or metal block placed adjacent to the pinhole entrance to their ion energy-angle analyzer. They observed that the IAD became asymmetric and the IED developed a low energy tail as the superwafer topography approached the pinhole from one side, in agreement with the model results discussed in this article.

ACKNOWLEDGMENTS

This work was supported by the Semiconductor Research Corporation, National Science Foundation (ECS 94-04133, CTS 94-12565), and the University of Wisconsin ERC for Plasma Aided Manufacturing.

[1]*Handbook of Plasma Processing Technology*, edited by S. M. Rossnagel, J. J. Cuomo, and W. D. Westwood (Noyes, Park Ridge, NJ, 1990).
[2]N. Hershkowitz (private communication, 1996).
[3]J. Holland, Lam Research Corp. (private communication, 1996).
[4]R. J. Hoekstra and M. J. Kushner, J. Appl. Phys. **77**, 3668 (1995).

[5]P. L. G. Ventzek, R. J. Hoekstra, and M. J. Kushner, J. Vac. Sci. Technol. B **12**, 461 (1994).
[6]W. Z. Collison and M. J. Kushner, Appl. Phys. Lett. **68**, 903 (1996).
[7]M. J. Grapperhaus and M. J. Kushner, J. Appl. Phys. **81**, 569 (1997).
[8]R. J. Hoekstra and M. J. Kushner, J. Appl. Phys. **79**, 2275 (1996).
[9]T. S. Cale, G. B. Raup, and T. H. Gandy, J. Vac. Sci. Technol. A **10**, 1128 (1992).
[10]V. K. Singh, E. S. G. Shaqfeh, and J. P. McVittie, J. Vac. Sci. Technol. B **10**, 1091 (1992).
[11]S. Hamaguchi and M. Dalvie, J. Electrochem. Soc. **141**, 1964 (1994).
[12]C. C. Cheng, K. V. Guinn, V. M. Donnelly, and I. P. Herman, J. Vac. Sci. Technol. A **12**, 2630 (1994).
[13]E. Meeks (unpublished).
[14]J. Zheng, R. P. Brinkman, and P. McVittie, J. Vac. Sci. Technol. A **13**, 859 (1995).